UKAEA-CCFE-PR(23)105

D. Padrao, D. Hancock, J. Paterson, F. Schoofs, C. Tuck, M. Magnini, I. Maskery

Investigating gyroid and primitive lattice structures for additively manufactured heat exchangers

Investigating gyroid and primitive lattice structures for additively manufactured heat exchangers

D. Padrao, D. Hancock, J. Paterson, F. Schoofs, C. Tuck, M. Magnini, I. Maskery

New structure-property relationships for surface-based lattice structures as candidates for heat exchangers

D. Padrão[a], D. Hancock[b], J. Paterson[b], F. Schoofs[b], C. Tuck[a], M. Magnini[c], I. Maskery[a,*]

[a]*Centre for Additive Manufacturing, University of Nottingham, Nottingham NG8 1BB, UK*
[b]*United Kingdom Atomic Energy Authority, Culham Science Centre, OX14 3DB, Abingdon, UK*
[c]*Fluids and Thermal Engineering Research Group, University of Nottingham, Nottingham NG7 2RD, UK*

Abstract

Heat exchangers have manifold applications, from micro-electronics to nuclear fusion reactors. Their performance expectations will continue to increase in line with the power consumption and miniaturisation of technology. Additive manufacturing enables the creation of novel, compact heat exchangers with greater surface-to-volume ratios and geometrical complexities than standard pin/fin arrays and pipes. Despite this, there has been little research into the use of high surface area lattice structures as heat exchangers. Here, the hydraulic and thermal performance of five surface-based lattice structures were examined numerically. CFD data were used to create useful predictive models for pressure drop and volumetric heat transfer coefficients over a range of flow rates and volume fractions, which can henceforth be used by heat transfer engineers. The thermal performance of surface-based lattices was found to be heavily dependent on internal geometry, with structures capable of distributing thermal energy across the entire fluid volume having greater volumetric heat transfer coefficients than those with only localised areas of high heat transfer and low levels of fluid mixing.

Keywords: Additive manufacturing, cellular structure, lattice, fluid flow, conjugate heat transfer, computational fluid dynamics (CFD)

1. Introduction

Additive manufacturing (AM) describes a range of processes which join materials to make solid parts from 3D model data, usually layer upon layer [1]. Metal AM offers enhanced design freedom compared to conventional processes, enabling the production of near-net shape components with complex internal geometries and high customisability, such that parts can be tailored for specific applications and users [2]. This technology was initially developed for rapid prototyping, but is now used in several sectors to produce final products, such as in aerospace [3] where the GE LEAP fuel nozzle has been a notable commercial success [4].

Alongside topology optimisation, the incorporation of 3D cellular structures is a key element of AM design. Ordered lattices (as opposed to the typically random foams that can be made with gas injection [5], for example) have received significant attention in the literature [6], and are now available in several commercial CAD packages aimed at AM. They reduce component weight, have high surface-to-volume ratios and high solid-fluid contact areas [2, 5], making metal lattices in particular ideal candidates for heat exchangers [7–9]. Compared to lattices composed of interconnected struts or 'trusses', triply periodic minimal surface (TPMS) lattices have enclosed channels for fluid flow, greater surface areas, and are generally stiffer and stronger at equivalent weight [10]. Therefore, TPMS lattices offer unique advantages for fluid flow and heat transfer applications, in addition to other niche applications such as intervertebral devices [11].

Heat exchangers are common devices with applications ranging from micro-electronics [12] to nuclear fusion [13]. Standard heat exchangers employ extended surfaces (such as fin arrays) with heat from the component being dissipated to a coolant. The dominant heat transfer mechanisms under laminar flow conditions are convective cooling in the fluid streamline direction and conduction in the direction normal to fluid flow. For turbulent flow, heat transfer is driven by convection in the fluid [14]. The large surface areas and complex geometries of TPMS lattice structures are therefore promising for heat transfer. Conversely, these features lead to greater pressure drop, and therefore potentially lower heat exchanger efficiency. This effect is seen in the work of Dixit *et al* [15], where a simple cubic strut lattice provided a lower heat transfer coefficient and pressure drop than more complex structures.

The need to dissipate large quantities of heat from small volumes will continue to increase in line with the increased power demands and miniaturisation of electronic devices. It is therefore necessary for heat exchangers to

---

*Corresponding author
Email address: `ian.maskery@nottingham.ac.uk` (I. Maskery)

ΔT_{LMTD}	Logarithmic mean temperature difference (K)	n	Parameter correlating Nu_{vol} to Re
$\dot{m}$	Mass flow rate $(kg\ s^{-1})$	Nu_{vol}	Volumetric Nusselt number
A_{ν}	Specific surface area (m^{-1})	P	Fluid pressure (Pa)
$A_{w,s}$	Wetted surface area (m^2)	Re	Reynolds number
c_p	Specific heat capacity $(J\ kg^{-1}\ K^{-1})$	$T_{f,in}$	Fluid inlet temperature (K)
D_h	Hydraulic diameter (m)	$T_{f,out}$	Fluid outlet temperature (K)
F	Parameter correlating Nu_{vol} to Re	T_h	Heater temperature (K)
h_l	Local wall heat transfer coefficient $(W\ m^{-2}\ K^{-1})$	T_s	Average channel surface temperature (K)
$h_{m,vol}$	Volumetric heat transfer coefficient $(W\ m^{-3}\ K^{-1})$	u_m	Mean channel fluid velocity $(m\ s^{-1})$
h_m	Global mean heat transfer coefficient $(W\ m^{-2}\ K^{-1})$	u_s	Superficial fluid velocity $(m\ s^{-1})$
K	Darcian permeability (m^2)	V_T	Total volume of design space (m^3)
k	Thermal conductivity $(W\ m^{-1}\ K^{-1})$	V_w	Wetted volume (m^3)
K_1	Forchheimer permeability (m^2)	**Greek letters**	
K_2	Inertial permeability (m)	γ	Volume fraction
L	Channel length (m)	μ	Dynamic viscosity $(kg\ m^{-1}\ s^{-1})$
		ν	Kinematic viscosity $(m^2\ s^{-1})$
		ρ	Density $(kg\ m^{-3})$

be maximally efficient, in terms of their size and material usage. Despite this, there has been little research on the use of complex surface-based cellular structures within AM heat exchangers, with much of the published work dedicated to foams [16–19], strut-based lattices [15, 20–23] or conventional pin/fin arrays and channels [22, 24–26]. Recently, heat transfer in TPMS structures has garnered some attention, with applications including heat exchangers [27–31], injection mold cooling [32] and latent heat thermal energy storage systems [33, 34].

Pulvirenti *et al* [27] conducted a numerical study into the gyroid matrix lattice at low Reynolds numbers. The authors found that the lattice structure was characterised by local volumetric heat transfer coefficients similar to those of other periodic structures, such as the Kelvin geometry [18, 19]. Santos *et al* [35] examined the permeability of a range of TPMS lattice structures and found that the fluid flow was described by the Darcy-Forchheimer law, which is helpful in identifying designs for efficient lattice-based heat exchangers. Concerning the permeability of foams, Della Torre *et al* [36] found an exponential dependence of the permeability on porosity, supporting the notion that porosity can be a useful design parameter

for specifying flow in analogous AM lattices. Maloney *et al* [20] found the thermal conductance of a micro-strut-based lattice heat exchanger to be determined by various geometrical features such as node-to-node spacing and lattice member diameter. These studies provide an overall framework to develop structure-property relationships for flow and heat transfer in AM cellular structures.

This paper examines the hydraulic and thermal transfer properties of TPMS-based lattice geometries over a range of fluid flow velocities and volume fractions. We establish design guides for fluid flow and heat transfer in these lattices in terms of their principal geometrical properties. Section 2 describes the methodology for our work, with sections 2.1, 2.2 and 2.3 providing details about the design of lattices and CFD modelling. Sections 3 and 4 contain the main results and discussion of this study. Concluding remarks are given in section 5.

2. Methodology

2.1. Cellular structures

Five TPMS lattice structures were chosen for this study. These were the diamond matrix (DM), gyroid ma-

trix (GM), lidinoid matrix (LM), primitive matrix (PM) and split-p matrix (SPM) lattices. The DM, GM and PM lattices were chosen as they have received the most attention in the literature, whereas the remaining structures were chosen for their tortuous channels and high surface areas. The examined structures are illustrated in figure 1.

Each examined structure had dimensions of $10 \times 50 \times 10$ mm containing $1 \times 5 \times 1$ lattice cells. These were chosen to provide sufficient surface to allow the fluid to develop fully and to examine the evolution of mixing arising from the periodicity of the structures. To develop general structure-performance models for arbitrary lattice geometries, the fluid dynamics within the lattice cells must first be understood. For this reason, the structures examined here comprise a single unit cell in the directions normal to fluid flow.

The TPMS lattice structures were generated using FLatt Pack, a research-focused lattice design program [37]. TPMS-based lattice structures can be subdivided into 'network' and 'matrix' forms, where the matrix forms were used in this study as they possess greater surface areas per unit volume [38]. A network phase lattice consists of two continuous regions, one solid and one void. A matrix phase lattice has three continuous regions, two of which are void with equivalent geometries, with the other being a solid separating wall. For heat exchange applications, network lattices can exchange heat between a solid and a fluid while matrix lattices can exchange heat between two fluids across a solid barrier. One of the key geometrical properties of TPMS lattice structures is volume fraction, γ, defined as the ratio between solid volume and design space volume. This can be controlled, for TPMS matrix lattices, by modifying the thickness of the walls. The volume fraction of the examined structures in this study ranged from $\gamma = 0.15 - 0.4$.

2.2. Computational Method

Computational fluid dynamics (CFD) was used here to model fluid flow and conjugate heat transfer. Numerical results were obtained using OpenFOAM v1812 [39], an open-source CFD software written in C++. A conjugate heat transfer solver, *chtMultiRegionSimpleFoam*, was used to model incompressible, steady-state fluid and heat transfer between different bodies, where the solid region is modelled with the heat conduction equation and the fluid-solid solutions are coupled at the common boundaries by imposing continuity of temperature and heat flux.

Our CFD models included a fluid domain of dimensions $10 \times 90 \times 10$ mm, which encapsulate the solid lattice test structure. Inlet and outlet pipes were used, 20 mm in length each. We found that this was sufficient for the flow to develop and transition in to the structures and that there were no divergent results at the lattice boundary. The *snappyHexMesh* utility was used to import STL representations of the lattice structures into the computational domain to provide CFD meshes. Finally, heat was applied to the lattice structure via a constant-temperature 'heater'

(dimensions $10 \times 50 \times 2$ mm) at 323 K at the base of the modelled domain. Heating was applied in one direction in order to be more closely analogous to real applications (e.g., liquid cooling of a CPU or GPU) and to examine the impact of a directional heat source. The schematics of the computational domain of a simple circular channel model (which was used for CFD validation) are given in figure 2.

Water was modelled in the fluid domain with a density, ρ, of 1,000 kg m^{-3}, a kinematic viscosity, ν, of 8.9×10^{-7} m^2 s^{-1} and assumed to be incompressible. The fluid travelled in the y-direction, with inlet flow rates of $u_s = 0.8 \times 10^{-3} - 6 \times 10^{-3}$ m s^{-1}, corresponding to $Re = 3.2 - 62.5$. This flow regime was examined to ensure that there would be significant differences between results at different flow rates and such that the performance of these structures can be meaningfully compared with other work in the literature, such as that of Pulvirenti *et al* [27] and Santos *et al* [35].

Flow in our CFD models was defined by the *noSlip* boundary condition (BC) at the walls and fluid boundaries, forcing the fluid velocity to zero, and the *pressureInletOutletVelocity* BC at the outlet, where a zero-gradient condition was applied for outflow. The inlet flow was defined by a *fixedValue* BC, which fixes the velocity to a specified value. The pressure at the outlet was defined by a *fixedValue* BC and the inlet was defined by a *fixedFluxPressure* BC, which sets the pressure gradient such that the flux is specified by the fluid velocity BC. The temperature of the fluid domain was defined by an *inletOutlet* BC of 293 K applied to the inlet fluid and a *zeroGradient* BC at the outlet. The solid domain was modelled as Inconel-718 (which has seen extensive use in heat exchangers in the aerospace industry [3]), with a density of 8,190 kg m^{-3}, specific heat capacity of 435 J kg^{-1} K^{-1} and a thermal conductivity of 11.4 W m^{-1} K^{-1}. These boundary conditions are well-established for finite-volume modelling and have been used to accurately predict fluid flow and heat transfer [19, 28, 36].

A CFD mesh convergence study was performed to determine a suitable mesh element density for accurate fluid flow and conjugate heat transfer predictions. This was performed for a GM lattice structure ($\gamma = 0.4$) at a volumetric flow rate of 6×10^{-7} m^3 s^{-1}. The pressure drop and outlet fluid temperature were found to be well converged at around 1.8 million elements, as shown in figure 3, for an unstructured mesh featuring refined polyhedral elements at the fluid-solid boundaries and hexahedral elements elsewhere (see figure 4). The models used throughout this work therefore feature similar meshes.

As discussed in section 2.3, the examined flow range is in the laminar-turbulent transition region. A convergence study was therefore performed for a GM lattice structure (γ=0.4) to determine whether a turbulence model was necessary to model the fluid accurately. The pressure drop for the RANS (Reynolds-averaged Navier-Stokes) k-ϵ turbulence model agreed with the DNS (direct numerical simulation, i.e., no turbulence model) results, as shown in
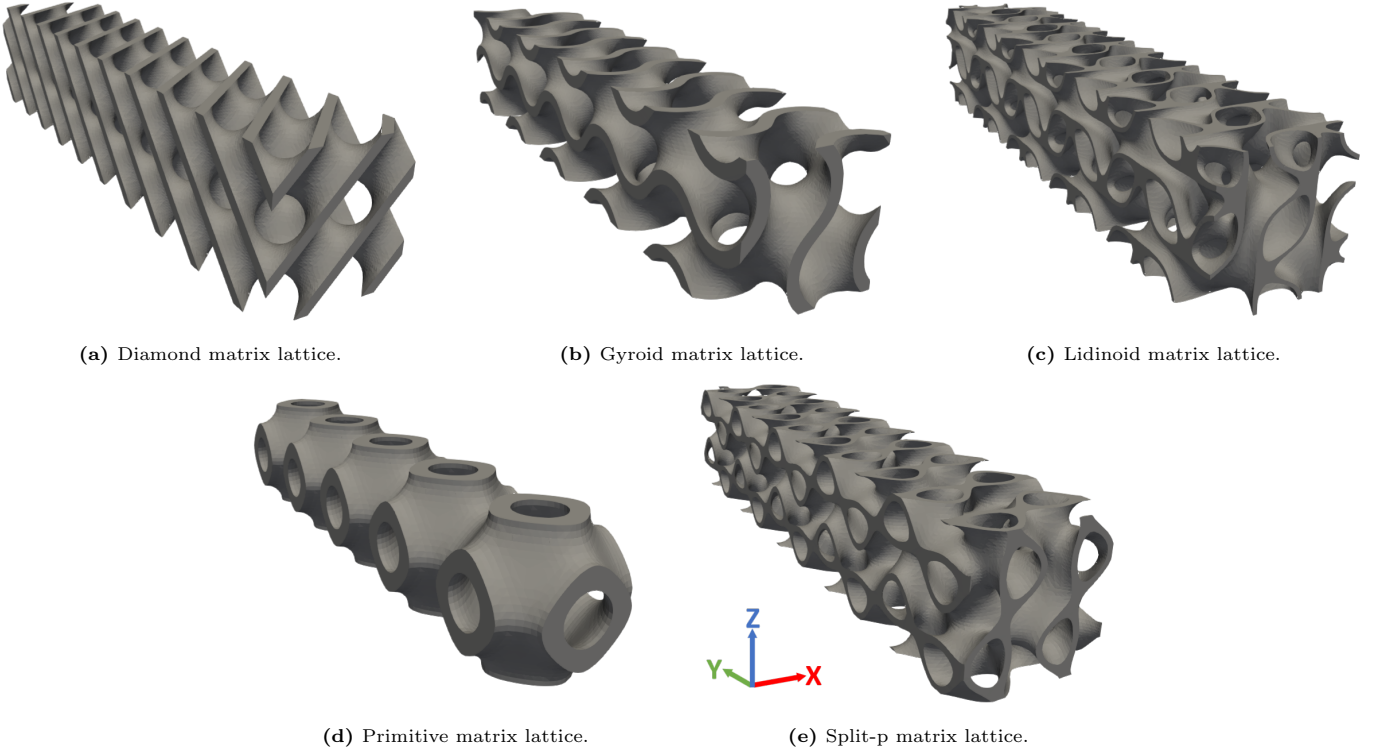
(a) Diamond matrix lattice.

(b) Gyroid matrix lattice.

(c) Lidinoid matrix lattice.

(d) Primitive matrix lattice.

(e) Split-p matrix lattice.

Figure 1: Examined structures (shown with a volume fraction of 0.25).

(a) Fluid domain.

(b) Cross-sectional view with the fluid domain (grey), solid domain (red) and heater (green).
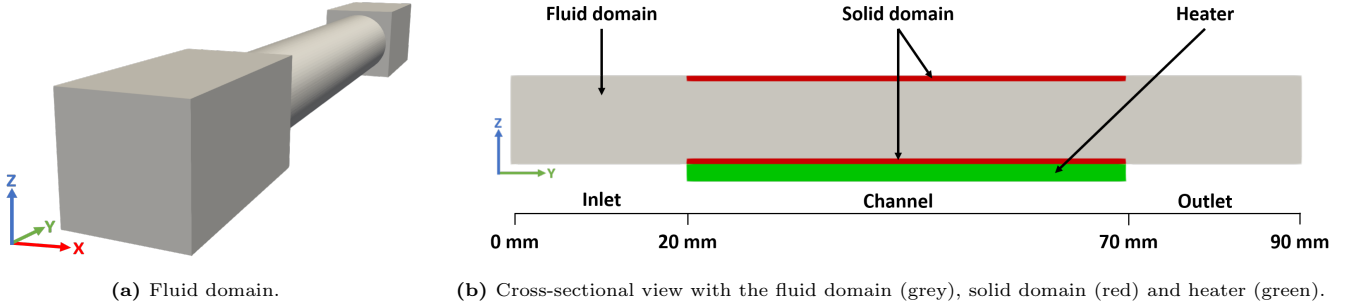
Figure 2: Schematics for the computational domain of a simple circular channel.
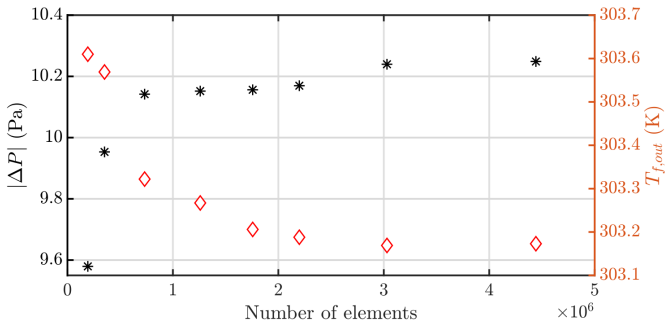

Figure 3: Pressure drop (black star) and outlet fluid temperature (red diamond) mesh convergence analysis for a gyroid matrix lattice (superficial fluid velocity = 6×10^{-3} m s^{-1}, volume fraction = 0.4).

figure 5, so a turbulence model was not implemented for this study.

Our CFD model was first validated against the numerical results presented by Pulvirenti *et al* [27], where we obtained differences of 1.4% and 0.01% for the pressure drop and fluid exit temperature, respectively, for an equivalent GM structure. For completeness, we used our CFD model to predict fluid flow in a simple circular channel. This was validated against the Hagen-Poiseuille law, with our numerical model predicting pressure drops within 1% of the analytical solution.

2.3. Theoretical background and method

Pressure drop, ΔP, across the test structures was examined to determine the hydraulic performance of each lattice type. In addition, the fluid dynamics and variation of fluid pressure within the structures were examined to understand the impact of different lattice geometries at equivalent volume fractions.
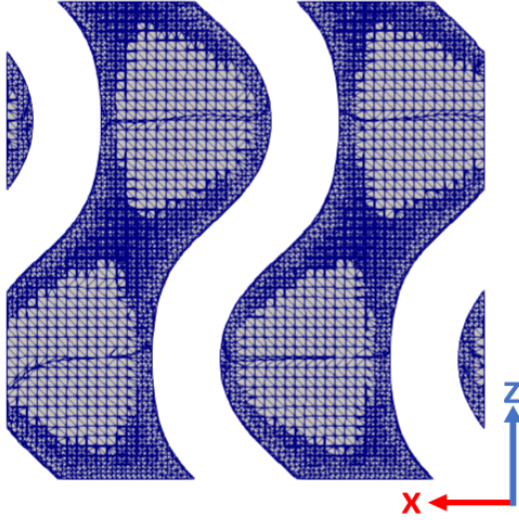
4

Figure 4: Mesh elements in the fluid domain for a gyroid matrix lattice with a volume fraction of 0.4 at a position $y=0.025$ m after the inlet.
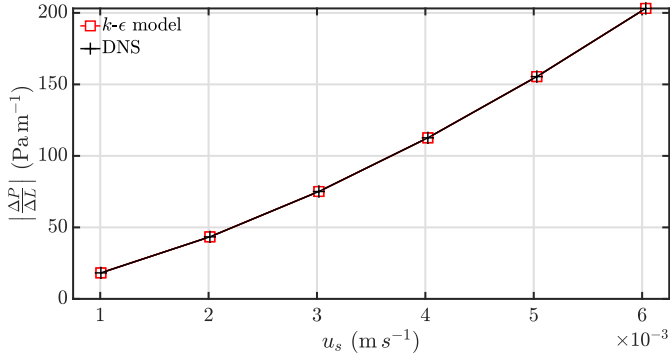

Figure 5: RANS and DNS pressure drop results for a gyroid matrix with a volume fraction of 0.4.

Darcy's law describes pressure drop across a porous medium for slow, viscous flow [35]

$$\left|\frac{\Delta P}{\Delta L}\right| = \frac{\mu}{K}u_s \, , \tag{1}$$

where $\Delta P/\Delta L$ is the pressure drop per unit length, μ is the dynamic viscosity, K is the Darcian permeability constant and u_s is the superficial fluid velocity. At high flow rates, where the flow is no longer in the Darcy regime, a non-linear term is added to account for inertial effects. This is known as the Forchheimer term [40]. We have

$$\left|\frac{\Delta P}{\Delta L}\right| = \frac{\mu}{K_1}u_s + \frac{\rho}{K_2}u_s{}^2 \, , \tag{2}$$

where K_1 is the Forchheimer permeability constant and K_2 is the inertial permeability constant. The permeability constants are in general associated with the geometry of the porous medium, where K and K_1 represent the vis-

cous drag and K_2 is linked to the blockage of the internal geometry [40]. It is important to note that K and K_1 are not the same. This is because transitioning from a Darcian to a Forchheimer flow regime implies changes to the viscous and inertial drags [40, 41]. It is vital to know which regime applies to the flow in a particular structure, in order to use the appropriate model. This was achieved by rearranging equation 2 to obtain

$$\left|\frac{\Delta P}{\Delta L\, u_s}\right| = \frac{\mu}{K_1} + \frac{\rho}{K_2}u_s \, , \tag{3}$$

which was then used to fit pressure drop data [40]; any part which is linear with u_s is Forchheimer flow.

Reynolds numbers are also quoted in this work as they provide more general descriptions of fluid flow and can be compared to other studies, which may use different initial conditions and geometries. The Reynolds number for a porous structure is [17]

$$Re = \frac{u_s\, D_h}{\nu\,(1-\gamma)} \, , \tag{4}$$

where D_h is the hydraulic diameter. The transition region between laminar and turbulent flow for porous structures exists for $10 < Re < 2000$ [42].

D_h for porous structures was calculated using [17]

$$D_h = 4\frac{V_w}{A_{w,s}} \, , \tag{5}$$

where V_w is the wetted volume and $A_{w,s}$ is the wetted surface area, which was extracted from the CAD representations of the lattice structures. This approach was used to estimate the hydraulic diameter as it takes into account the complexity of different lattice types across the entire fluid domain. Different lattice types therefore experience different Reynolds numbers at equivalent inlet flow rates, which more accurately reflects the fluid flow compared to the assumption of equal Re.

Heat transfer performance was examined through mass flow rate weighted averages of heat transfer coefficients and Nusselt numbers. Two different heat transfer coefficients were used, the first being a local wall heat transfer coefficient, h_l. This was calculated directly in OpenFOAM using the Reynolds analogy model, which relates the wall shear stress to heat transfer [43, 44]. Due to it being a local variable, it can be used to determine points of high and low heat transfer within the examined structures.

The global, mean heat transfer coefficient, h_m, was also examined. It is given by [15]

$$h_m = \frac{\dot{m}c_p\,(T_{f,out} - T_{f,in})}{A_{w,s}\Delta T_{LMTD}} \, , \tag{6}$$

where $\dot{m}$ is the fluid mass flow rate, c_p is the fluid specific heat capacity, $T_{f,out}$ and $T_{f,in}$ are the fluid outlet and inlet temperatures and ΔT_{LMTD} is the logarithmic mean

temperature difference. ΔT_{LMTD} was given by

$$\Delta T_{LMTD} = \frac{T_{f,out} - T_{f,in}}{\ln\left(\frac{T_h - T_{f,in}}{T_h - T_{f,out}}\right)}, \qquad (7)$$

where T_h is the heater temperature. This definition of ΔT_{LMTD} has been used previously by Dixit *et al.* [15], but an alternative definition uses the average channel surface temperature, T_s, in place of T_h [19, 22]. T_h was used here because $T_h - T_{f,in}$ gives the initial temperature difference in the structures [34], whereas using T_s gives the heat transfer over the entire fluid-solid interface, the size of which varies significantly between lattice designs. T_s is also not representative of the large distribution of surface temperatures present in TPMS lattice structures, as observed by Al-Ketan *et al* [29].

In this study, the volumetric heat transfer coefficient, $h_{m,vol}$, was used instead of h_m as it is independent of the surface area (which differs for different lattice structures at equivalent volume fraction). This was obtained from [18]

$$h_{m,vol} = h_m A_\nu, \qquad (8)$$

where A_ν is the specific surface area (ratio of wetted surface area to design space volume).

The volumetric Nusselt number gives the ratio of convective to conductive heat transfer for a fluid and is an alternative way to express heat transfer performance. This was defined by [18]

$$Nu_{vol} = \frac{h_{m,vol} D_h{}^2}{k}, \qquad (9)$$

where k is the thermal conductivity of the fluid. This is a dimensionless quantity and can be used alongside Re to compare structures under different flow conditions.

3. Results

3.1. Hydraulic Performance

Pressure drop for a range of volume fractions and flow rates are presented in figure 6, where ΔP is calculated by finding the difference between inlet and outlet average pressure. Figure 6 shows that ΔP increases non-linearly with both u_s and γ and that the LM lattice exhibits the greatest pressure drop across the examined ranges while the PM lattice exhibits the lowest pressure drop in most cases.

At low volume fractions the GM lattice exhibits greater pressure drop than the PM structure. This behaviour switches at a critical volume fraction, indicating that a particular lattice geometry may not be treated as inherently more efficient than others, with performance also being dependent on fluid flow conditions.

Examining the evolution of fluid pressure, taken as a cross-sectional average (figure 7), we see that pressure decreases linearly along the flow direction in the GM, DM
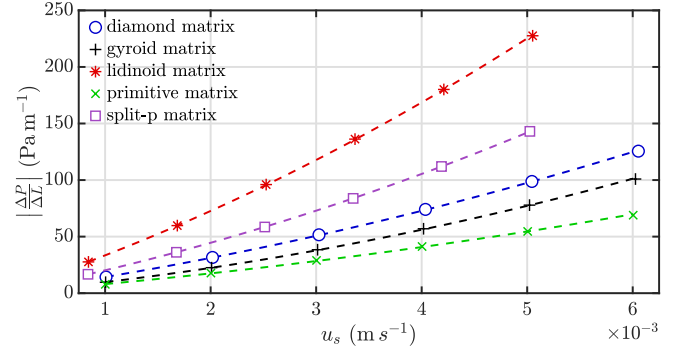
(a) Pressure drop for structures with a volume fraction of 0.25. The $(--)$ lines represent equation 2.
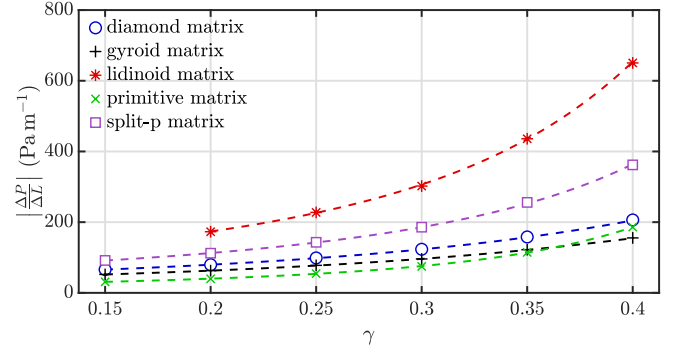
(b) Pressure drop for structures with a superficial fluid velocity of 5×10^{-3} m s^{-1}. The $(--)$ lines represent equation 12.

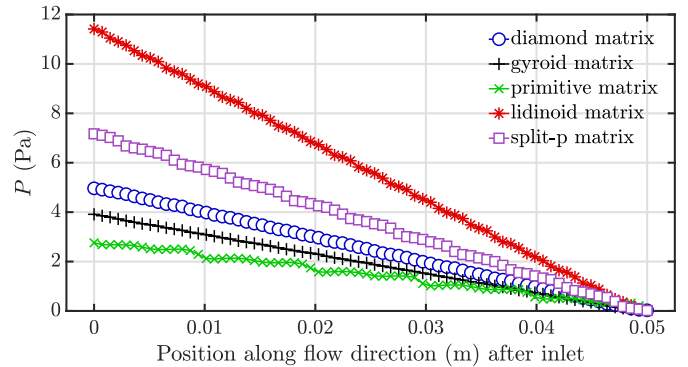**Figure 6:** Pressure drop for different examined geometries.

Figure 7: Evolution of pressure within the examined structures (superficial fluid velocity $= 5 \times 10^{-3}$ m s^{-1}, volume fraction $= 0.25$).

and LM structures, despite the tortuous nature of the channels. This is not replicated in the PM or SPM structures, which instead exhibit more periodic pressure drops.

This can be explained by examining the flow within the structures, as shown in figure 8. Regarding the PM structure, the majority of the fluid passes through a central volume or 'channel'. However, as the channel diameter decreases at the cell boundary, some fluid is recirculated in the characteristic chambers of the PM lattice, appearing as eddies. The PM geometry therefore acts as a series of bottlenecks, providing sharp pressure drops within the structure. This can also be observed in the SPM lattice, but to a lesser degree. Flow is not periodically impeded in
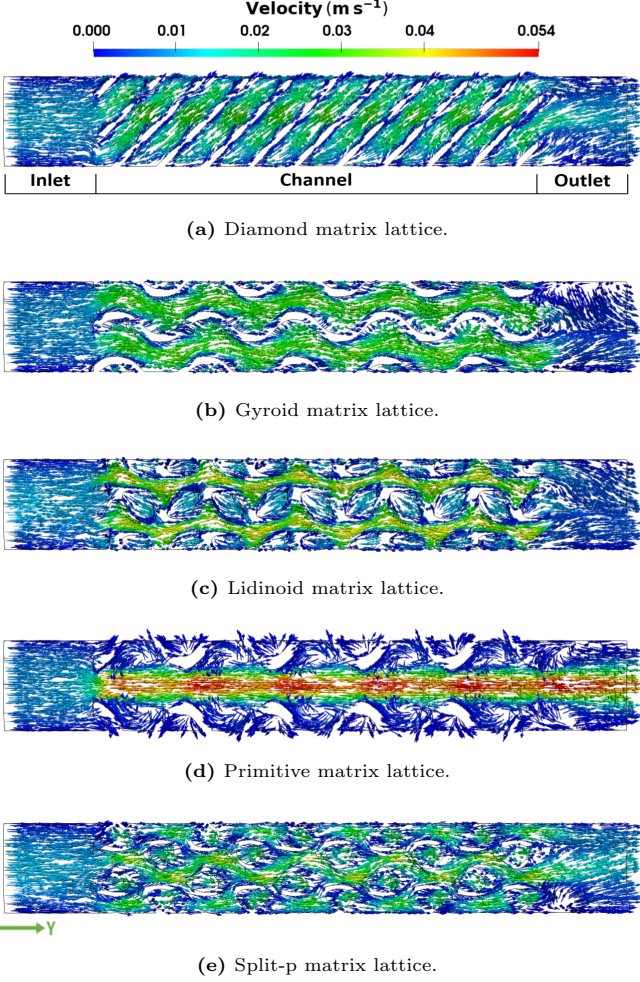
(a) Diamond matrix lattice.

(b) Gyroid matrix lattice.

(c) Lidinoid matrix lattice.

(d) Primitive matrix lattice.

(e) Split-p matrix lattice.

Figure 8: Fluid velocity vectors across the $x = 0.005$ m plane for structures with a volume fraction of 0.25 and a superficial fluid velocity of 5×10^{-3} m s^{-1}.

the remaining structures because their internal geometry does not possess such large variations in channel diameter, minimising fluid recirculation. The dominant factor behind pressure drop for TPMS structures is therefore the channel diameter, where smaller channels lead to larger pressure drops, shown in figure 9, and where changes in the diameter lead to localised pressure drops.

Before calculating the permeability constants, the flow regime must be determined. We found $\Delta P/(\Delta L\, u_s)$ to increase linearly with u_s for each lattice over the range of examined volume fractions, indicating that the flow is in the Forchheimer regime. $\Delta P/\Delta L$ were therefore fit with equation 2 to determine the permeability constants for each lattice structure, which are plotted in figure 10. K_2 are four orders of magnitude larger than K_1, with both constants decreasing as volume fraction increases. Figure 10 shows that at low volume fractions, the PM structure exhibits larger K_1 and K_2 than the GM structure. This switches at a critical volume fraction, which is $\gamma \sim 0.3$ for K_1, and we observe the approach of this change at $\gamma = 0.4$ for K_2. Therefore, the critical volume fraction responsible for the
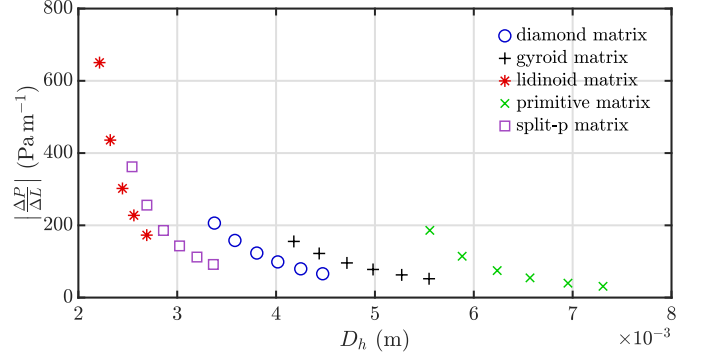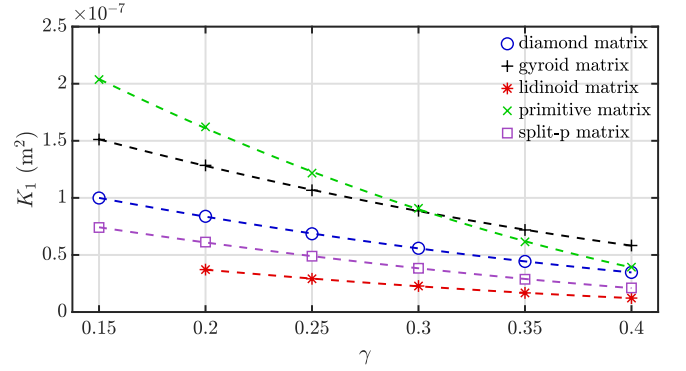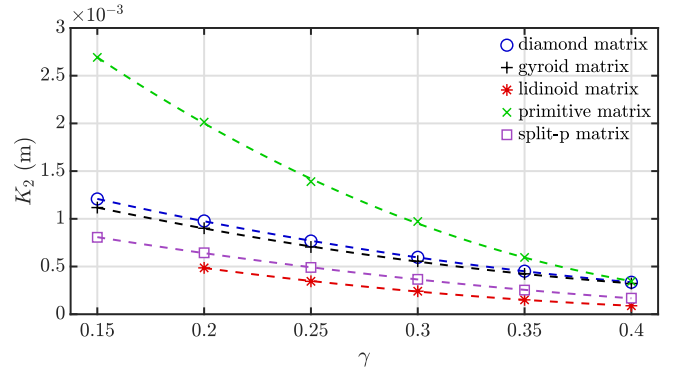

Figure 9: Pressure drop for structures with a superficial fluid velocity of 5×10^{-3} m s^{-1}.

(a) Forchheimer permeability constant. The $(--)$ lines represent equation 10.

(b) Inertial permeability constant. The $(--)$ lines represent equation 11.

Figure 10: Permeability constants as a function of volume fraction for different lattice geometries.

intersection of pressure drop behaviour in figure 6(b) is in the range of 0.3 - 0.4, irrespective of fluid velocity.

For each examined lattice type, the following equations

$$K_1 = A_1\gamma^2 + B_1\gamma + C_1\,, \tag{10}$$

$$K_2 = A_2\gamma^2 + B_2\gamma + C_2 \tag{11}$$

were used to relate K_1 and K_2 to the volume fraction, γ, where $A_{1,2}$, $B_{1,2}$ and $C_{1,2}$ are fit parameters. Equation 2

7

can then be expressed as

$$\left|\frac{\Delta P}{\Delta L}\right| = \frac{\mu\, u_s}{A_1\gamma^2 + B_1\gamma + C_1} + \frac{\rho\, u_s{}^2}{A_2\gamma^2 + B_2\gamma + C_2}\,, \quad (12)$$

which can be used to predict the pressure drop exhibited by each structure over a range of volume fractions and superficial fluid velocities. Equation 12 describes a surface, where figure 11 compares the hydraulic performance of the GM and PM lattices. Fit values for the parameters are given in table 1, which can henceforth be used to specify the volume fraction for the examined TPMS structures to provide a pressure drop for a known flow rate.

3.2. Thermal performance

Volumetric Nusselt numbers are presented in figure 12. Correlations of the form

$$Nu_{vol} = F\, Re^n \qquad (13)$$

were sought, where Fu *et al* [18] stated that the parameters n and F are related to the geometrical features of the structure. Figure 12 shows that this relationship describes the data accurately. Equations 9 and 13 are then combined to provide

$$h_{m,vol} = \frac{F\, k\, Re^n}{D_h{}^2}\,, \qquad (14)$$

which is valuable because it can be expressed in terms of u_s and γ. This is done using equations 4 and 5, while D_h can also be defined as

$$D_h = 4\frac{V_w}{A_{w,s}} = 4\frac{\left(V_w/V_T\right)}{\left(A_{w,s}/V_T\right)} = \frac{4}{A_\nu}\left(1-\gamma\right), \qquad (15)$$

where V_T is the total volume of the design space. Equation 14 can therefore be expressed as

$$\begin{aligned}
h_{m,vol} &= F\, k\, D_h{}^{n-2}\left(\frac{u_s}{\nu\left(1-\gamma\right)}\right)^n, \\
&= F\, k\left(\frac{4}{A_\nu}\right)^{n-2}\left(1-\gamma\right)^{n-2}\left(\frac{u_s}{\nu\left(1-\gamma\right)}\right)^n, \\
&= F\, k\left(\frac{4}{A_\nu}\right)^{n-2}\left(\frac{u_s}{\nu}\right)^n\left(1-\gamma\right)^{-2}. \quad (16)
\end{aligned}$$

To use equation 16 as a predictive model for $h_{m,vol}$ over a range of fluid velocities and volume fractions, the dependence of A_ν, n and F on volume fraction must be known. It was found that A_ν and n decrease with volume fraction, and are well described by $A_\nu = p_1\gamma^{p_2} + p_3$ and $n = n_1\gamma + n_2$. We observed no discernible relationship between F and γ, but, for each lattice type, the full range of F values was seen to fall within $\overline{F} \pm 8\%$. Therefore, F was treated as a constant by calculating its mean value. The volumetric heat transfer coefficient can then
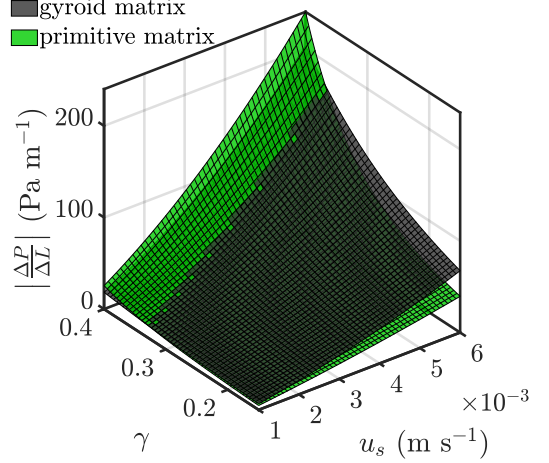

Figure 11: Pressure drop as a function of superficial fluid velocity and volume fraction for the gyroid matrix and primitve matrix lattice.
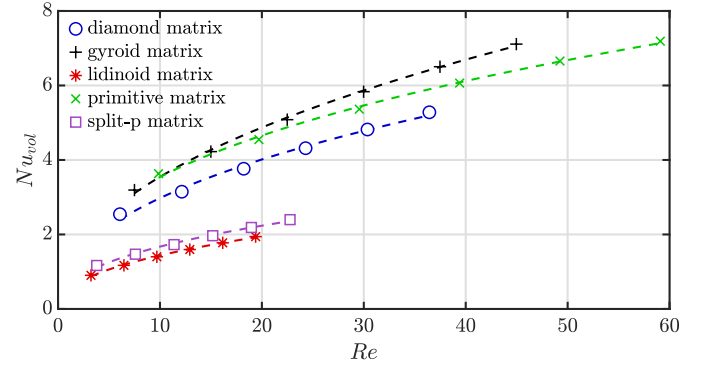

Figure 12: Volumetric Nusselt numbers for lattice structures with a volume fraction of 0.25. The $(--)$ lines represent equation 13.

be obtained from

$$h_{m,vol} = \frac{\overline{F}\, k\left(\dfrac{4}{p_1\gamma^{p_2} + p_3}\right)^{n_1\gamma + n_2 - 2}\left(\dfrac{u_s}{\nu}\right)^{n_1\gamma + n_2}}{\left(1-\gamma\right)^2}\,, \quad (17)$$

with $p_{1,2,3}$, $\overline{F}$ and $n_{1,2}$ given in table 2. This equation describes a surface and can be used to predict the volumetric heat transfer coefficient over a range of volume fractions and superficial fluid velocities. This model accurately predicts the $h_{m,vol}$ from our numerical models, with a maximum deviation less than 10% over the examined ranges of volume fraction and flow rate.

Figure 13 displays the volumetric heat transfer coefficient exhibited by each lattice structure predicted by equation 17. The LM lattice exhibits the greatest volumetric heat transfer coefficient at low volume fractions, but at higher volume fractions the DM lattice has the highest volumetric heat transfer coefficient. An interesting feature was observed for the GM and SPM lattices, where the intersection of $h_{m,vol}$ is dependent on both the volume fraction and superficial fluid velocity. The PM lattice

Lattice type	Fit parameter $\times 10^{-7}$ (m^2)				Fit parameter $\times 10^{-3}$ (m)			
	A_1	B_1	C_1	Adjusted R^2	A_2	B_2	C_2	Adjusted R^2
DM	3.4	-4.5	1.59	0.9999	5.9	-6.8	2.09	0.9999
GM	4.7	-6.3	2.35	0.9998	6.0	-6.5	1.95	0.9998
LM	2.1	-2.5	0.79	0.9995	4.9	-4.9	1.27	0.9994
PM	10.1	-12.1	3.63	0.9997	22.3	-21.6	5.44	0.9994
SPM	2.6	-3.6	1.22	0.9998	3.9	-4.7	1.42	0.9998

Table 1: Determined fit parameters for equation 12.

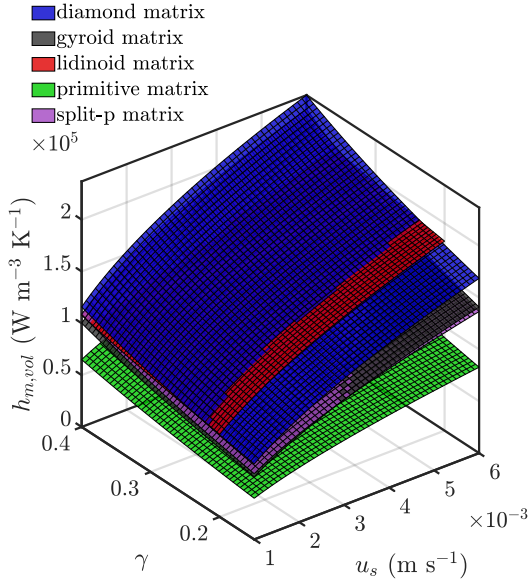| Lattice type	p_1 (m^{-1})	p_2	p_3 (m^{-1})	Adjusted R^2	$\overline{F}$	n_1	n_2	Adjusted R^2
DM	-405	2.13	768	0.9999	1.06	-0.277	0.510	0.8812
GM	-308	2.09	619	0.9998	1.21	-0.173	0.499	0.9738
LM	-847	1.92	1232	0.9990	0.52	-0.455	0.554	0.9987
PM	-305	2.23	471	0.9998	1.39	-0.135	0.431	0.9709
SPM	-580	2.13	1026	0.9999	0.63	-0.106	0.444	0.8733

Table 2: Determined fit parameters for equation 17.

Figure 13: Volumetric heat transfer coefficient as a function of superficial fluid velocity and volume fraction.

Figure 14: Evolution of local wall heat transfer coefficient within the examined structures (superficial fluid velocity = 5×10^{-3} m s^{-1}, volume fraction = 0.25).

exhibits the lowest volumetric heat transfer coefficient in this study.

Local properties are important in determining how the lattice geometry affects heat transfer. h_l were calculated across 70 equally spaced cross-sections along the flow direction and are shown in figure 14. All of the TPMS structures exhibit periodically fluctuating h_l, with the PM lattice showing the g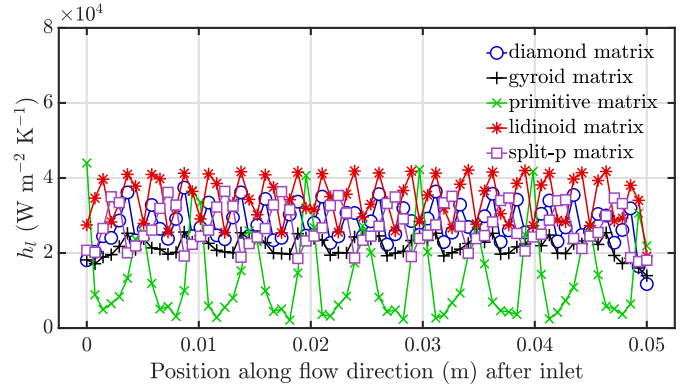reatest variation in h_l, from 2,100 to 44,000 W m^{-2} K^{-1}. Despite having the highest h_l, the PM structure also has the lowest h_l which explains why it exhibits the lowest $h_{m,vol}$. The other lattice structures have much smaller variance in h_l.

The distribution of h_l on the lattice surface further explains the differences observed in figure 14. For simplicity and brevity, figure 15 displays the distribution of h_l for the PM lattice only, which was chosen due to the large variation in h_l. Peak h_l are seen in regions where the channel diameter is narrowest in the central 'channel'. Other high h_l regions are observed outside the central 'channel', where the channel is at a local minima. The fluid moves faster in these sections, as shown in figure 8(d), and can there-
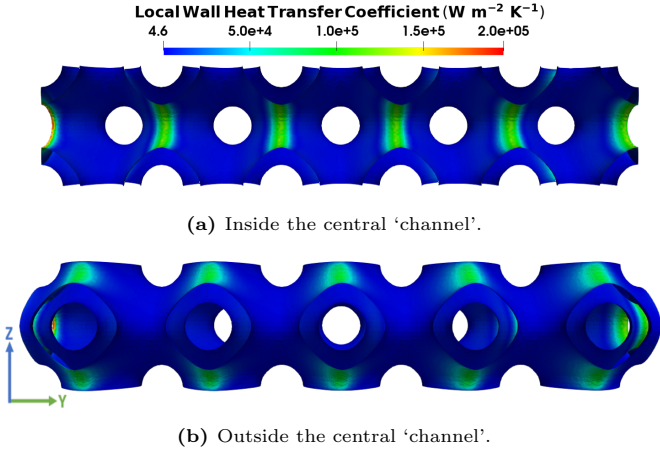
9

(a) Inside the central 'channel'.

(b) Outside the central 'channel'.

Figure 15: Distribution of local wall heat transfer coefficient in the primitive matrix lattice (superficial fluid velocity $= 5 \times 10^{-3}$ m s^{-1}, volume fraction $= 0.25$).

(a) Forchheimer permeability constant. The $(--)$ lines represent equation 10.

(b) Inertial permeability constant. The $(--)$ lines represent equation 11.

Figure 16: Permeability constants of the gyroid matrix and primitive matrix structures of the current study, gyroid and primitive matrix structures [35] and a foam structure [17].

fore transport more heat away from the walls there. The same effect is also observed in the other examined TPMS structures. h_l is therefore driven by the local fluid velocity, which itself is largely determined by the channel diameter.

4. Discussion

4.1. Hydraulic performance

Santos *et al* [35] calculated the permeability constants for a variety of lattice structures consisting of $4 \times 4 \times 4$ cells in a $13 \times 13 \times 13$ mm volume over a range of different flow regimes. Compared to the structures in the present study, those lattices have greater surface area and a larger number of cells per unit volume, and we can therefore expect the structures of Santos *et al* [35] to be less permeable than the lattice structures examined here within the Forchheimer flow region. This is confirmed in figure 16, where the permeability constants, K_1 and K_2, for the gyroid and primitive matrix lattices in this study are up to two orders of magnitude greater than those of Santos *et al* [35]. This highlights the challenge of developing general and practicable analytical relationships for the flow in these structures, as a range of geometrical properties, such as the number of cells and size of the design space, clearly have a large impact on the permeability. However, the work of Santos *et al* [35] confirms our observation that the primitive matrix lattice is more permeable at lower volume fractions and the gyroid matrix is more permeable at larger volume fractions. This finding was further elaborated in the current study by examining the fluid dynamics (see figure 8) and evolution of pressure drop (see figure 7) within the structures. Sharp pressure drops were found in the primitive matrix lattice at the cell boundaries, while the gyroid matrix lattice does not exhibit this behaviour.

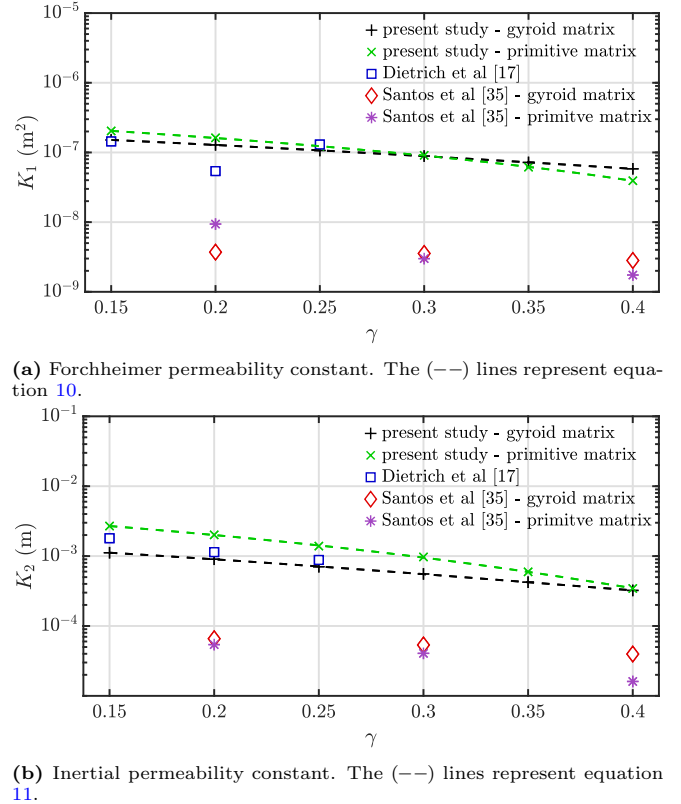Dietrich *et al* [17] calculated the permeability constants for foams of different materials with varying pore sizes and volume fractions. A selection of those results are compared to this study in figure 16. The gyroid and primitive matrix lattices possess permeabilities similar to manufactured foam. Additively manufactured surface-based lattices can therefore be a valid substitute for conventional foams in fluid flow applications, as they are hydraulically no less efficient and also possess a greater degree of tailorability due to their computer-based design method.

The Forchheimer and inertial permeabilities of lattice structures are dependent on the internal geometry, and therefore, quite clearly, the volume fraction. The fits used here (equations 10 and 11) are empirical, and do not account specifically for such factors as surface area or channel tortuosity, either of which may be found to have a predominant effect on fluid flow. A robust, general model will incorporate these, and other, geometrical factors into structure-property relationships capable of accurately predicting fluid through any lattice type. We have made a contribution towards this goal with equation 12 and the parameters quoted in table 1. These can be used to predict pressure drop over a range of volume fractions and superficial fluid velocities for the examined lattice structures. This will enable designers to make informed decisions on lattice design for fluid flow applications. These fit parameters are valid only for structures with $1 \times 5 \times 1$ cells for a design space of $10 \times 50 \times 10$ mm. These results are

still valuable however, since flow in larger lattice structures (i.e., $N_1 \times N_2 \times N_3$ cells) is determined to a large extent by the characteristic fluid dynamics in individual cells.

4.2. Thermal performance

As discussed previously, the local wall heat transfer coefficient is ultimately dependent on the channel diameter. It is therefore expected that surface-based lattice structures exhibit volumetric heat transfer coefficients which mirror their pressure drop behaviour in figure 9, where structures with smaller hydraulic diameters have larger pressure drops. This is not the case however as, for example, the diamond matrix lattice exhibits relatively small pressure drops but high volumetric heat transfer coefficients.

By examining the distribution of fluid temperature in the primitive matrix lattice in figure 17, we see that there is minimal thermal mixing within the structure due to the high-velocity central flow channel (shown in figure 8(d)) which prevents the fluid from moving across it. It is also observed that there is minimal heat transfer taking place in the upper regions where the local volumetric heat transfer coefficient peaks (figure 15). This is because heat is applied to the structure only from one direction (below). Therefore, structures which (i) conduct more heat through the lattice walls far away from the heat input, and (ii) maximise thermal mixing, should boast greater volumetric heat transfer coefficients.

This theory is corroborated by the distribution of fluid outlet temperature in figure 18. Here, we observe that the primitive matrix lattice, which has the lowest volumetric heat transfer coefficient, has the least well distributed fluid outlet temperature and that the top half of the structure is rendered relatively ineffective for heat transfer. Following on from this, the gyroid matrix and split-p matrix lattices have the next highest volumetric heat transfer coefficients and more evenly distributed fluid outlet temperatures, though a discontinuity are still observed between the bottom and top halves of those structures. Finally, the diamond and lidinoid matrix lattices have the highest volumetric heat transfer coefficients in this study and have relatively well distributed fluid outlet temperatures indicating better fluid mixing.

We conclude that the thermal performance of TPMS lattice structures is heavily dependent on the internal geometry of the structure in the case of a directional heat input, where lattices that can distribute heat across the entire fluid volume exhibit greater performance. In the case of a non-directional heat input (i.e., fixed wall temperatures) the thermal performance will be largely determined by the diameters of the channels within the structure. This is in keeping with the emerging picture from investigations of TPMS lattices as heat exchangers; their thermal performance is heavily dependent on lattice cell geometry [29].

Nusselt numbers for foams were previously examined by Wu *et al* [19] and Fu *et al* [18], who employed the
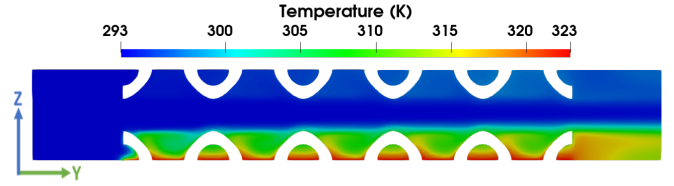

Figure 17: Fluid temperature across the $x = 0.005$ m plane for the primitive matrix lattice (superficial fluid velocity $= 5 \times 10^{-3}$ m s^{-1}, volume fraction $= 0.25$).

relationship given in equation 13. The excellent agreement with this model for the lattice structures examined here (figure 12) confirms that these surface-based lattices can be characterised by volumetric Nusselt numbers in the same way as conventional foams. A robust, general model will be able to predict the thermal performance of surface-based lattices across a range of superficial fluid velocities and volume fractions. Equation 17 and the parameters quoted in table 2 contribute to this and can accurately predict the volumetric heat transfer coefficient for the examined surface-based lattice structures with $1 \times 5 \times 1$ cells in a $10 \times 50 \times 10$ mm design space. This model can be improved, and generalised to other lattice structures, by incorporating more complete descriptions of how the Nusselt parameters F and n are affected by the internal lattice geometry.

Combined with the model discussed above for hydraulic performance, surface-based lattice structures can henceforth be designed in a way which minimises their pressure drop for a given flow rate whilst achieving a specified heat transfer coefficient. This can be achieved via a simple search-based algorithm applied to their pressure drop and heat transfer relationships (i.e., the surfaces given by equations 12 and 17). The practical implication of reduced pressure drop for a given flow rate is reduced power consumption for the pumps, or fans, which move the coolant through the heat exchanger. Being able to design surface-based heat exchangers which reduce or maintain power consumption compared to traditional designs, whilst improving heat transfer capabilities, will be important for various applications which require enhanced cooling.

5. Conclusions

This work examines the fluid flow and conjugate heat transfer of five surface-based lattices suitable for additively manufactured heat exchangers. Permeability constants for the lattice structures were calculated and used to create a predictive model for pressure drop over a range of fluid velocities and volume fractions. Relationships between volumetric Nusselt number and Reynolds number were also found and can be used to predict volumetric heat transfer coefficients for examined structures across a range of fluid velocities and volume fractions. With these models, heat exchangers based on the examined lattice structures
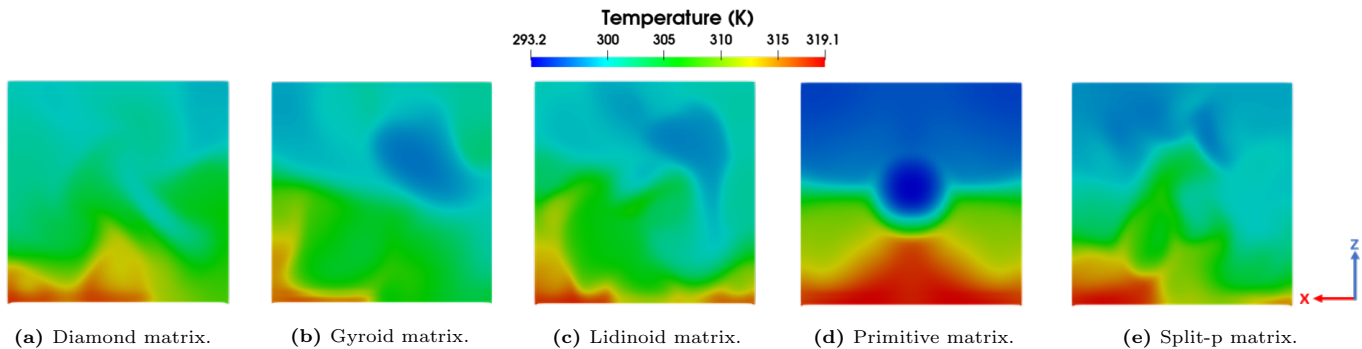
Temperature (K)
293.2 300 305 310 315 319.1

(a) Diamond matrix.   **(b)** Gyroid matrix.   **(c)** Lidinoid matrix.   **(d)** Primitive matrix.   **(e)** Split-p matrix.

Figure 18: Distribution of outlet fluid temperature (superficial fluid velocity $= 5 \times 10^{-3}$ m s^{-1}, volume fraction $= 0.25$).

can be designed to meet pre-defined performance requirements. The investigative method used in the current study can be applied across the large, and ever-increasing, family of lattice structures for heat exchangers without expensive manufacturing and testing.

The complex internal geometries of the lattice structures cause mixing and eddy formation, meaning they can be effective heat exchangers. However, analysis of flow and fluid temperature distributions indicate that the primitive matrix lattice examined here is a poorer candidate for heat management than the other four structures, as fluid mixing is impeded by the formation of a high-velocity central flow channel. Lattice structures which are able to distribute heat across the entire fluid volume, such as the diamond matrix, are much better candidates for heat management as they maximise fluid-solid thermal interactions and fluid mixing.

Structure-performance relationships of the kind uncovered here can be used in conjunction with other such rules, like the Gibson-Ashby scaling laws for stiffness or thermal conductivity [6], to design multifunctional components which, for example, provide maximal stiffness and thermal transport within a given weight restriction. New lattice structures for efficient heat exchangers can be identified, or even designed from first-principles, with greater understanding of their flow and heat transfer mechanisms. Such optimised surface-based heat exchangers can only be manufactured via additive manufacturing and can therefore be embedded in components of arbitrary geometry without the need for subsequent joining or assembly processes.

Acknowledgement

References

[1] ISO/ASTM 52900, "Additive manufacturing — General principles — Terminology," 2018. [Online]. Available: https://www.iso.org/obp/ui/{#}iso:std:iso-astm:52900:dis:ed-2:v1:en

[2] I. Gibson, D. Rosen, and B. Stucker, *Additive manufacturing technologies: 3D printing, rapid prototyping, and direct digital manufacturing, second edition*, 2nd ed., D. W. D. W. Rosen and B. B. Stucker, Eds. New York: Springer, 2015.

[3] B. Blakey-Milner, P. Gradl, G. Snedden, M. Brooks, J. Pitot, E. Lopez, M. Leary, F. Berto, and A. du Plessis, "Metal additive manufacturing in aerospace: A review," *Materials & Design*, vol. 209, p. 110008, nov 2021. [Online]. Available: https://linkinghub.elsevier.com/retrieve/pii/S0264127521005633

[4] General Electric, "New manufacturing milestone: 30,000 additive fuel nozzles," oct 2018. [Online]. Available: https://www.ge.com/additive/stories/new-manufacturing-milestone-30000-additive-fuel-nozzles

[5] M. F. Ashby, *Metal foams : a design guide*, M. F. Ashby, Ed. Oxford: Butterworth-Heinemann, 2000.

[6] L. J. Gibson, *Cellular solids : structure and properties*, 2nd ed., ser. Cambridge solid state science series, M. F. Ashby, Ed. Cambridge: Cambridge University Press, 1997.

[7] H. N. Wadley and D. T. Queheillalt, "Thermal Applications of Cellular Lattice Structures," *Materials Science Forum*, vol. 539-543, pp. 242–247, mar 2007. [Online]. Available: http://www.scientific.nethttps://www.scientific.net/MSF.539-543.242

[8] T. Lu, H. Stone, and M. Ashby, "Heat transfer in open-cell metal foams," *Acta Materialia*, vol. 46, no. 10, pp. 3619–3635, jun 1998. [Online]. Available: https://linkinghub.elsevier.com/retrieve/pii/S1359645498000317

[9] J. Tian, T. Lu, H. Hodson, D. Queheillalt, and H. Wadley, "Cross flow heat exchange of textile cellular metal core sandwich panels," *International Journal of Heat and Mass Transfer*, vol. 50, no. 13-14, pp. 2521–2536, jul 2007. [Online]. Available: www.elsevier.com/locate/ijhmthttps://linkinghub.elsevier.com/retrieve/pii/S0017931007000129

[10] O. Al-Ketan, R. Rowshan, and R. K. Abu Al-Rub, "Topology-mechanical property relationship of 3D printed strut, skeletal, and sheet based periodic metallic cellular materials," *Additive Manufacturing*, vol. 19, pp. 167–183, jan 2018. [Online]. Available: https://doi.org/10.1016/j.addma.2017.12.006https://linkinghub.elsevier.com/retrieve/pii/S2214860417303767

[11] A. Timercan, V. Sheremetyev, and V. Brailovski, "Mechanical properties and fluid permeability of gyroid and diamond lattice structures for intervertebral devices: functional requirements and comparative analysis," *Science and Technology of Advanced Materials*, vol. 22, no. 1, pp. 285–300, dec 2021. [Online]. Available: https://www.tandfonline.com/doi/full/10.1080/14686996.2021.1907222

[12] B. Jasperson, Yongho Jeon, K. Turner, F. Pfefferkorn, and Weilin Qu, "Comparison of Micro-Pin-Fin and Microchannel Heat Sinks Considering Thermal-Hydraulic Performance and Manufacturability," *IEEE Transactions on Components and Packaging Technologies*, vol. 33, no. 1, pp. 148–160, mar 2010. [Online]. Available: http://ieeexplore.ieee.org/document/5286856/

[13] D. Hancock, D. Homfray, M. Porton, I. Todd, and B. Wynne,

"Exploring complex high heat flux geometries for fusion applications enabled by additive manufacturing," *Fusion Engineering and Design*, vol. 136, pp. 454–460, 2018.

[14] J. H. Ferziger, M. Perić, and R. L. Street, *Computational Methods for Fluid Dynamics*, 4th ed. Cham: Springer International Publishing, 2020. [Online]. Available: http://link.springer.com/10.1007/978-3-319-99693-6

[15] T. Dixit, P. Nithiarasu, and S. Kumar, "Numerical evaluation of additively manufactured lattice architectures for heat sink applications," *International Journal of Thermal Sciences*, vol. 159, p. 106607, jan 2021. [Online]. Available: https://linkinghub.elsevier.com/retrieve/pii/S1290072920310577

[16] Z. Wu, C. Caliot, F. Bai, G. Flamant, Z. Wang, J. Zhang, and C. Tian, "Experimental and numerical studies of the pressure drop in ceramic foams for volumetric solar receiver applications," *Applied Energy*, vol. 87, no. 2, pp. 504–513, feb 2010. [Online]. Available: https://linkinghub.elsevier.com/retrieve/pii/S0306261909003122

[17] B. Dietrich, W. Schabel, M. Kind, and H. Martin, "Pressure drop measurements of ceramic sponges-Determining the hydraulic diameter," *Chemical Engineering Science*, vol. 64, pp. 3633–3640, 2009.

[18] R. Viskanta, X.Fu and J. Gore, "Measurement and correlation of volumetric heat transfer coefficients of cellular ceramics," *Experimental Thermal and Fluid Science*, vol. 17, no. 4, pp. 285–293, aug 1998. [Online]. Available: https://linkinghub.elsevier.com/retrieve/pii/S089417779810002X

[19] Z. Wu, C. Caliot, G. Flamant, and Z. Wang, "Numerical simulation of convective heat transfer between air flow and ceramic foams to optimise volumetric solar air receiver performances," *International Journal of Heat and Mass Transfer*, vol. 54, no. 7-8, pp. 1527–1537, mar 2011. [Online]. Available: https://linkinghub.elsevier.com/retrieve/pii/S0017931010006514

[20] K. J. Maloney, K. D. Fink, T. A. Schaedler, J. A. Kolodziejska, A. J. Jacobsen, and C. S. Roper, "Multifunctional heat exchangers derived from three-dimensional micro-lattice structures," *International Journal of Heat and Mass Transfer*, vol. 55, no. 9-10, pp. 2486–2493, apr 2012. [Online]. Available: https://linkinghub.elsevier.com/retrieve/pii/S0017931012000129

[21] J. Ho, K. Leong, and T. Wong, "Additively-manufactured metallic porous lattice heat exchangers for air-side heat transfer enhancement," *International Journal of Heat and Mass Transfer*, vol. 150, p. 119262, apr 2020. [Online]. Available: https://linkinghub.elsevier.com/retrieve/pii/S0017931019355140

[22] M. Wong, I. Owen, C. Sutcliffe, and A. Puri, "Convective heat transfer and pressure losses across novel heat sinks fabricated by Selective Laser Melting," *International Journal of Heat and Mass Transfer*, vol. 52, no. 1-2, pp. 281–288, jan 2009. [Online]. Available: https://linkinghub.elsevier.com/retrieve/pii/S0017931008003311

[23] S. M. Thompson, Z. S. Aspin, N. Shamsaei, A. El-wany, and L. Bian, "Additive manufacturing of heat exchangers: A case study on a multi-layered Ti–6Al–4V oscillating heat pipe," *Additive Manufacturing*, vol. 8, pp. 163–174, oct 2015. [Online]. Available: http://dx.doi.org/10.1016/j.addma.2015.09.003https://linkinghub.elsevier.com/retrieve/pii/S2214860415000469

[24] C. K. Stimpson, J. C. Snyder, K. A. Thole, and D. Mongillo, "Roughness Effects on Flow and Heat Transfer for Additively Manufactured Channels," *Journal of Turbomachinery*, vol. 138, no. 5, may 2016. [Online]. Available: https://asmedigitalcollection.asme.org/turbomachinery/article/doi/10.1115/1.4032167/378649/Roughness-Effects-on-Flow-and-Heat-Transfer-for

[25] K. L. Kirsch and K. A. Thole, "Pressure loss and heat transfer performance for additively and conventionally manufactured pin fin arrays," *International Journal of Heat and Mass Transfer*, vol. 108, pp. 2502–2513, may 2017. [Online]. Available: https://linkinghub.elsevier.com/retrieve/pii/S0017931016337243

[26] A. J. Wildgoose, K. A. Thole, P. Sanders, and L. Wang, "Impact of Additive Manufacturing on Internal Cooling Channels With Varying Diameters and Build Directions," *Journal of Turbomachinery*, vol. 143, no. 7, jul 2021. [Online]. Available: https://asmedigitalcollection.asme.org/turbomachinery/article/143/7/071003/1101298/Impact-of-Additive-Manufacturing-on-Internal

[27] B. Pulvirenti, M. Celli, and A. Barletta, "Flow and Convection in Metal Foams: A Survey and New CFD Results," *Fluids*, vol. 5, no. 3, p. 155, sep 2020. [Online]. Available: https://www.mdpi.com/2311-5521/5/3/155

[28] R. Attarzadeh, M. Rovira, and C. Duwig, "Design analysis of the "Schwartz D" based heat exchanger: A numerical study," *International Journal of Heat and Mass Transfer*, vol. 177, p. 121415, oct 2021. [Online]. Available: https://linkinghub.elsevier.com/retrieve/pii/S0017931021005184

[29] O. Al-Ketan, M. Ali, M. Khalil, R. Rowshan, K. A. Khan, and R. K. Abu Al-Rub, "Forced Convection Computational Fluid Dynamics Analysis of Architected and Three-Dimensional Printable Heat Sinks Based on Triply Periodic Minimal Surfaces," *Journal of Thermal Science and Engineering Applications*, vol. 13, no. 2, apr 2021. [Online]. Available: https://asmedigitalcollection.asme.org/thermalscienceapplication/article/doi/10.1115/1.4047385/1084162/Forced-Convection-Computational-Fluid-Dynamics

[30] Z. Cheng, R. Xu, and P.-X. Jiang, "Morphology, flow and heat transfer in triply periodic minimal surface based porous structures," *International Journal of Heat and Mass Transfer*, vol. 170, p. 120902, may 2021. [Online]. Available: https://doi.org/10.1016/j.ijheatmasstransfer.2021.120902https://linkinghub.elsevier.com/retrieve/pii/S0017931021000053

[31] J. Kelly, L. Finkenauer, P. Roy, J. Stolaroff, D. Nguyen, M. Ross, A. Hoff, and J. Haslam, "Binder jet additive manufacturing of ceramic heat exchangers for concentrating solar power applications with thermal energy storage in molten chlorides," *Additive Manufacturing*, vol. 56, p. 102937, aug 2022. [Online]. Available: https://doi.org/10.1016/j.addma.2022.102937https://linkinghub.elsevier.com/retrieve/pii/S2214860422003335

[32] S.-H. Oh, J.-W. Ha, and K. Park, "Adaptive Conformal Cooling of Injection Molds Using Additively Manufactured TPMS Structures," *Polymers*, vol. 14, no. 1, p. 181, jan 2022. [Online]. Available: https://www.mdpi.com/2073-4360/14/1/181

[33] Z. A. Qureshi, S. A. B. Al Omari, E. Elnajjar, F. Mahmoud, O. Al-Ketan, and R. A. Al-Rub, "Thermal characterization of 3D-Printed lattices based on triply periodic minimal surfaces embedded with organic phase change material," *Case Studies in Thermal Engineering*, vol. 27, p. 101315, oct 2021. [Online]. Available: https://linkinghub.elsevier.com/retrieve/pii/S2214157X21004780

[34] Z. A. Qureshi, E. Elnajjar, O. Al-Ketan, R. A. Al-Rub, and S. B. Al-Omari, "Heat transfer performance of a finned metal foam-phase change material (FMF-PCM) system incorporating triply periodic minimal surfaces (TPMS)," *International Journal of Heat and Mass Transfer*, vol. 170, p. 121001, may 2021. [Online]. Available: https://linkinghub.elsevier.com/retrieve/pii/S0017931021001046

[35] J. Santos, T. Pires, B. P. Gouveia, A. P. Castro, and P. R. Fernandes, "On the permeability of TPMS scaffolds," *Journal of the Mechanical Behavior of Biomedical Materials*, vol. 110, p. 103932, oct 2020. [Online]. Available: https://doi.org/10.1016/j.jmbbm.2020.103932

[36] A. Della Torre, G. Montenegro, G. Tabor, and M. Wears, "CFD characterization of flow regimes inside open cell foam substrates," *International Journal of Heat and Fluid Flow*, vol. 50, pp. 72–82, dec 2014. [Online]. Available: https://linkinghub.elsevier.com/retrieve/pii/S0142727X14000642

[37] I. Maskery, L. Parry, D. Padrão, R. Hague, and I. Ashcroft, "FLatt Pack: A research-focussed lattice design program," *Additive Manufacturing*, vol. 49, p. 102510, jan 2022. [Online]. Available: https://linkinghub.elsevier.com/retrieve/pii/S2214860421006576

[38] O. Al-Ketan, D.-W. Lee, R. Rowshan, and R. K. Abu Al-Rub,

"Functionally graded and multi-morphology sheet TPMS lattices: Design, manufacturing, and mechanical properties," *Journal of the Mechanical Behavior of Biomedical Materials*, vol. 102, p. 103520, feb 2020. [Online]. Available: https://linkinghub.elsevier.com/retrieve/pii/S1751616119312482

[39] "OpenFOAM." [Online]. Available: https://www.openfoam.com/

[40] N. Dukhan and C. A. Minjeur, "A two-permeability approach for assessing flow properties in metal foam," *Journal of Porous Materials*, vol. 18, no. 4, pp. 417–424, aug 2011. [Online]. Available: http://link.springer.com/10.1007/s10934-010-9393-1

[41] S. Ergun, "Fluid flow through packed columns," *Chem. Eng. Progress.*, vol. 48, pp. 89–94, 1952.

[42] M. J. M. J. Rhodes, *Introduction to particle technology*, 2nd ed., ProQuest (Firm), Ed. Chichester, England ; Hoboken, NJ: Wiley, 2008.

[43] F. P. Incropera and D. P. DeWitt, *Fundamentals of Heat and Mass Transfer*, 6th ed. Hoboken, N.J. : Wiley, 2007.

[44] S. P. Mahulikar and H. Herwig, "Fluid friction in incompressible laminar convection: Reynolds' analogy revisited for variable fluid properties," *The European Physical Journal B*, vol. 62, no. 1, pp. 77–86, mar 2008. [Online]. Available: http://link.springer.com/10.1140/epjb/e2008-00115-0